Polymer, Water, and Salt Partitioning in Complex Coacervates Characterized by Femtosecond Stimulated Raman Microscopy

Francisco van Riel Neto, Carolin Borbeck, Torben Henning Saatkam, Maxine Kenny, Stephan Schmidt, Peter Gilch

Chemistry—Methods

Research Article
doi.org/10.1002/cmtd.202500005

Chemistry Europe
European Chemical Societies Publishing

www.chemistrymethods.org

Polymer, Water, and Salt Partitioning in Complex Coacervates Characterized by Femtosecond Stimulated Raman Microscopy

Francisco van Riel Neto, Carolin Borbeck, Torben Henning Saatkamp, Maxine Kenny, Stephan Schmidt, and Peter Gilch*

Complex coacervates can form through liquid–liquid phase separation in aqueous solutions containing oppositely charged macromolecules. This process results in macromolecule-rich droplets (coacervate phase) coexisting with a macromolecule-depleted supernatant phase. Here, femtosecond stimulated Raman microscopy (FSRM) is introduced as a tool to rapidly analyze both the supernatant and coacervate phases of complex coacervates. The well-known polyelectrolyte pair poly(diallyldimethylammonium chloride) and poly(4-styrenesulfonate) is investigated. Coacervate formation is induced by the addition of KBr and NH_4SCN as a Raman-active salt. For both salts, the partitioning of polymer and water between the coacervate droplets and the supernatant phase is quantified. For the Raman-active salt NH_4SCN, its partitioning between phases was also monitored. NH_4SCN was found to be enriched in the coacervate phase, as confirmed by FTIR spectroscopy. Overall, FSRM proves to be a valuable tool for collecting new data on coacervate composition requiring only low sample volumes and simple sample preparation, while offering convenient data acquisition.

1. Introduction

Coacervation is a phenomenon in which a homogenous solution undergoes liquid–liquid phase separation (LLPS), resulting in the formation of liquid droplets (**Figure 1**) rich in macromolecules coexisting with a continuous (supernatant) phase, where the macromolecules are depleted.[1,2] The droplets formed through this process are known as coacervates. If the phase separation process involves only one macromolecule, the phenomenon is referred to as simple coacervation. When two or more macromolecules are involved, it is termed complex coacervation.[1,2]

Coacervation occurs in samples containing both biological and synthetic macromolecules.[1–4] In biology, coacervates are used as a model system to study the formation of membraneless organelles,[5] in the synthesis of proteinaceous biomaterials such as spider silks[6] and underwater adhesives used by sandcastle worms and mussels.[7] Also, it is proposed that coacervation played an important role in the origin of life, due to their ability to form compartmentalized structures without the need for a membrane.[8] Coacervates also have different industrial applications, including their use as additives and emulsifiers in food,[9–11] underwater adhesives,[7,11,12] drug delivery,[13] and encapsulation.[14–16]

Complex coacervation is an associative type of LLPS that occurs in solutions containing macromolecules with opposite charges. Different charged macromolecules can be used in this process, such as proteins, polymers, colloids, and surfactants.[1] In this work, two oppositely charged polymers (polyelectrolytes) were used. The phase behavior of complex coacervates crucially depends on the salt concentration (Figure 1). For very low concentrations, a solid consisting of the two polyelectrolytes (a polyelectrolyte complex (PEC)) is formed and is in equilibrium with a liquid phase (not shown in Figure 1). For somewhat higher salt concentration, the polyelectrolyte-depleted supernatant phase is in equilibrium with a polyelectrolyte-rich liquid phase. For even higher salt concentration, beyond the critical point, the two phases coalesce in one liquid phase. The salt concentration in the two equilibrated phases (coacervate and supernatant) usually differs. An early theoretical treatment of this partitioning by Voorn and Overbeeck[17] favors an enrichment in the polymer-rich phase, as shown in the schematic phase diagram representation in Figure 1. Recent experiments and theoretical frameworks indicate that this is not always the case.[1,18]

Different experimental techniques to measure the polymer and salt content in coacervates, such as conductivity measurements,[19–21] UV-vis spectroscopy,[19,20] fluorescence (labeling) spectroscopy,[22,23] thermogravimetric analysis,[21,24,25] NMR spectroscopy[25,26] and radiolabeling,[27] have been used, either in combination or independently. Radiolabeling has also been utilized to measure the concentration of different salt ions inside PECs.[28,29] Numerous challenges have to be addressed to use

F. van Riel Neto, C. Borbeck, T. H. Saatkamp, M. Kenny, P. Gilch
Institut für Physikalische Chemie
Heinrich-Heine-Universität Düsseldorf
Universitätsstr. 1., 40225 Düsseldorf, Germany
E-mail: gilch@hhu.de

S. Schmidt
Institut für Makromolekulare Chemie
Albert-Ludwigs-Universität Freiburg
Stefan-Meier-Str. 31., 79104 Freiburg, Germany

Supporting information for this article is available on the WWW under https://doi.org/10.1002/cmtd.202500005

Research Article
doi.org/10.1002/cmtd.202500005
Chemistry Europe
European Chemical Societies Publishing

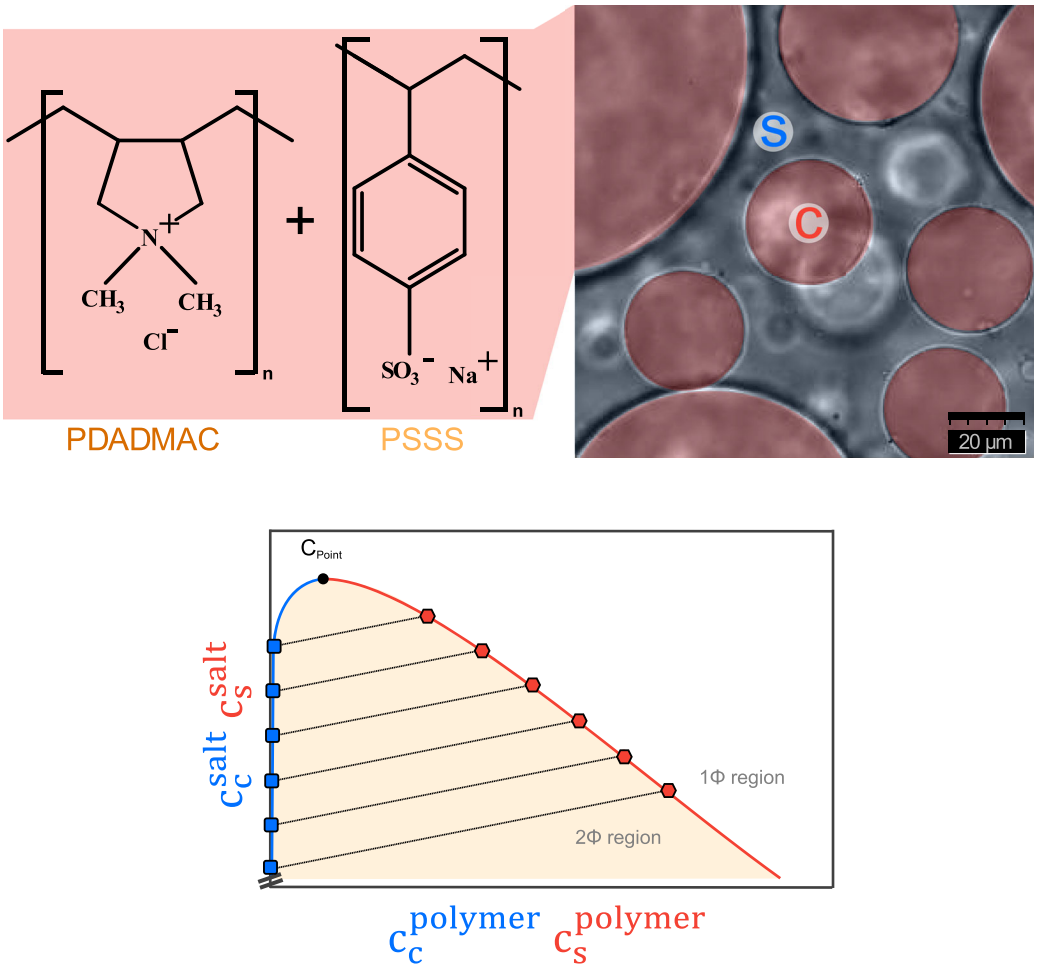

Figure 1. Complex coacervation and its dependence on polymer and salt concentrations. In the micrograph at the top right, coacervates (droplets marked in red) surrounded by the supernatant are shown. Structures of the coacervates forming polymers PDADMAC and PSS are shown on the left. The schematic phase diagram at the bottom indicates the phase behavior of complex coacervates according to the Voorn–Overbeek theory.[1,17] Salt and polymer concentrations of the supernatant phase are indicated in blue; those of the coacervate phase are in red. The tie lines (dashed) connect the two phases in equilibrium. Note that according to Voorn–Overbeek theory, these lines point upwards.

these techniques for the study of coacervation, often involving complex sample preparation. Coacervates are kinetically evolving systems, where coacervate droplets continuously coalesce over time, making it challenging to clearly distinguish and define the phase boundaries. Also, the phase separation process may yield a low quantity of coacervates or occur in a dilute solution, making it challenging to characterize both phases simultaneously. This challenge typically requires separating the supernatant and coacervate phases through centrifugation,[19–21,24,30] which often demands relatively large sample volumes. Also, processes that compete with LLPS, such as aggregation or fibrillization in the case of coacervate formed by proteins, can occur during the centrifugation, making it difficult to correctly assess the concentrations in the coacervate phase.[30,31] Many techniques also use fluorescent labeling to study coacervate samples, but the addition of fluorescent markers can interfere with the dynamics of the formation of coacervate droplets.[32] Additionally, for coacervate formation involving biological samples like proteins, the sample amount is often limited, favoring the use of microscopy methods. Many of the techniques described above are sensitive to either salt or polymer concentration. A technique reporting on both concentrations and, for consistency, also on the water content would be helpful. Additionally, the water content in the coacervate phase is relevant for the application of coacervates in encapsulation or drug delivery, since the cargo-carrying and cargo-release capacities of a coacervate droplet can be predicted based on the level of hydration of the coacervate droplets.[33]

Raman microscopy is of particular interest here as it can identify and quantify water and polymer content. In a pioneering study, Maeda et al.[34] characterized the polymer and water concentrations in phase-separated droplets and the surrounding supernatant in aqueous solutions of poly(N-isopropylacrylamide) (PNIPA). Recently, Choi et al.[35] used Raman microscopy to study the conformation of proteins and the structure of water in LLPS protein droplets. Raman spectroscopy and microscopy techniques were also used to reveal preferential pH conditions for protein complex coacervation[36] and study protein concentration inside and outside LLPS droplets[32] and to study the structure and concentration of water inside coacervate samples.[37,38] Using conventional (spontaneous) Raman microscopy has drawbacks in terms of

signal levels and, concomitantly, acquisition times.[39] Also, background fluorescence poses a significant challenge for conventional Raman microscopy. This fluorescence can reduce the signal-to-noise ratio (SNR) and, in extreme cases, completely obscure the Raman signal. The issue is particularly pronounced when studying biological samples using Raman spectroscopy.[40]

This challenge can be mitigated by nonlinear approaches such as coherent anti-Stokes Raman scattering (CARS) microscopy[39,41–43] and stimulated Raman scattering (SRS) microscopy.[39,44,45] Nonlinear Raman techniques benefit from the significantly larger cross section compared to spontaneous, which reduces acquisition times.[39] Also, for nonlinear Raman techniques, the fluorescence background is mitigated.[46] In this study, we used a variant of SRS microscopy—femtosecond stimulated Raman microscopy (FSRM).[44,47]

For this proof-of-principle experiment, a classic complex coacervate-forming pair consisting of the polycation poly(diallyldimthylammonium chloride) (PDADMAC) and the polyanion sodium poly(4-styrenesulfonate) (PSS) (for structures, see Figure 1) was studied.[20,25,48] Commonly, the salt concentration is adjusted using salts consisting of atomic ions. Often K^+ and Br^- are used, but these ions do not exhibit a vibrational Raman effect. Thus, for this study, a salt composed of the molecular ions NH_4^+ and SCN^- was selected. This salt was chosen because the SCN^- ion has a Raman band at 2064 cm^{-1},[49] which is separated from the Raman signals of the polymer and water. With this approach, FSRM was used to quantify the polymer, water, and salt contents in the coacervate and supernatant phases of PDADMAC/PSS coacervate samples, using only a small amount of sample (≈20 μL).

In the remainder of this article, first, FSRM experiments on coacervates formed by PDADMAC/PSS, KBr, and water are presented. FSRM records Raman spectra for every spatial pixel; using uni- and multivariate analysis, the respective datasets are converted into chemical maps depicting polymer and water content of the two phases. By averaging the contribution of the two phases, the contents are quantified. Second, coacervates obtained by mixing PDADMAC/PSS, NH_4SCN, and water are characterized. The same procedure as above is applied, but now also the distribution of the salt NH_4SCN is obtained. Raman-based results on the salt partitioning are confirmed by Fourier transform infrared spectroscopy (FTIR).

2. Results

As this study aims to measure concentrations in two different phases, we start out with introducing the respective physical measurands. Total concentrations $c_t^{\text{salt, polymer}}$ of salt and polymer are described by the amount of substance added to the total volume, which refers to the volume used to obtain the coacervate sample. All polymer concentrations refer to repeat units of polycations or polyanions, which are identical (see Experimental Section). Due to enrichments or depletions, the concentration in the coacervate $c_c^{\text{salt, polymer}}$ and supernatant $c_s^{\text{salt, polymer}}$ phases will differ from the total concentration. These concentrations are related by volume fractions ϕ_c for the coacervate phase and ϕ_s for the supernatant phase (Equation (1)),

$$c_t^{\text{salt,polymer}} = c_c^{\text{salt, polymer}}\phi_c + c_s^{\text{salt,polymer}}\phi_s \quad (1)$$

It is hereby assumed that upon phase separation the total volume is conserved.

To determine the polymer, water, and salt content in both the supernatant and coacervate phases, the Raman spectra acquired for each phase were analyzed based on the magnitude of the Raman bands associated with each component. In **Figure 2**a, the Raman spectrum of deionized water is shown. The broad Raman band that ranges from ≈3011 to 3609 cm^{-1} is composed of the different O—H stretching modes of the water molecules.[50,51] Figure 2b depicts the Raman spectrum of a NH_4SCN solution in water. The water Raman band is again visible in the ≈3011–3609 cm^{-1} region, and the peak at 2064 cm^{-1} is due to the stretching mode of SCN^-.[49] The Raman peaks associated with NH_4^+ overlap with the water peaks and are not clearly visible. Raman spectra of PSS and PDADMAC solutions in water are shown in Figure 2c,d. The spectra feature C—H stretching modes at ≈2952 cm^{-1} for PDADMAC and ≈2886 cm^{-1} for PSS.[52] The PSS spectrum also contains a band due to the aromatic C—H stretching mode at 3043 cm^{-1}. In Figure 2e, the sum of the PDADMAC and PSS spectra is compared with a suitable scaled spectrum of the coacervate phase obtained from a coacervate sample measurement (Figure 7). Within noise, these two spectra are identical, indicating that the interaction of the two polymers in the coacervate does not affect their Raman signatures.

To connect with an earlier study,[20] coacervate formation involving PDADMAC and PSS was first induced using KBr. It was possible to obtain phase separation for a concentration range of $c_t^{\text{KBr}} = 1.50$–1.66 M, for a fixed $c_t^{\text{polymer}} = 0.039$ M. Small volumes (≈20 μL) of these samples were first inspected by transmission microscopy to locate coacervate droplets. Then, areas of ≈100 × 100 μm^2 were scanned, and Raman spectra were obtained for each spatial pixel, which are separated by ≈1 μm. These datasets were converted into chemical maps (**Figure 3**) first using univariate analysis (more details in the Experimental Section). Hereby, the spectral integrals marked in Figure 3c,d were relied on. The values of these integrals are color-coded in Figure 3. In both maps, coacervate droplets surrounded by the supernatant are clearly discernible. The map quantifying the C—H stretching integral (Figure 3a) distinctly shows the expected higher polymer concentration within the droplet. The map based on the O—H stretching modes integral in Figure 3b indicates a lower water content in the droplet compared to the supernatant.

For the chemical map based on the C—H stretching (Figure 3a), the diameter of the droplet was measured to be ≈39.1 μm. For the O—H chemical map (Figure 3b), the diameter for the same droplet is ≈42.1 μm. Given the similar size of the coacervate droplets observed in both chemical maps, univariate analysis reliably distinguishes coacervate and supernatant phases.

To quantify the amounts of polymer and water in both the coacervate and supernatant phases, a multivariate analysis was

Research Article
doi.org/10.1002/cmtd.202500005
Chemistry Europe
European Chemical Societies Publishing

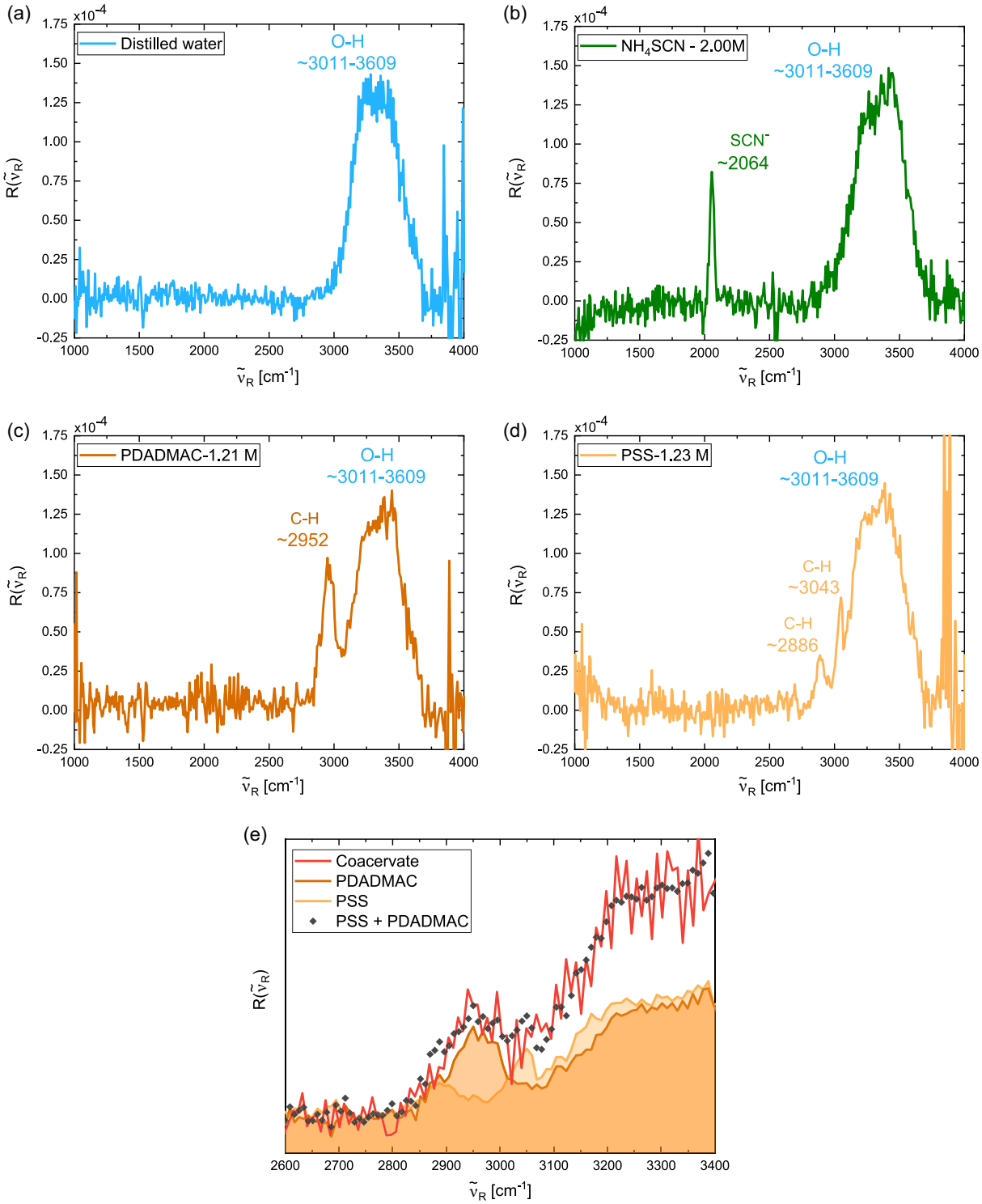

Figure 2. Raman spectra of the LLPS components. All spectra were obtained with the FSRM instrument. a) Distilled water, solutions of b) NH_4SCN (2.00 M), c) PDADMAC (1.21 M), and d) PSS (1.21 M) in water. e) Sum of the PDADMAC and PSS spectra compared with a scaled Raman spectrum of the coacervate phase obtained from a $c_t^{NH_4SCN} = 1.25$ M coacervate sample.

conducted using hierarchical cluster analysis. The method used is described in more detail in the Experimental Section. The approach was applied to the dataset used to generate the maps in Figure 3. The cluster to which each spectrum in the Raman dataset was attributed is represented in either red or blue. The red cluster (**Figure 4**) represents the coacervate droplet, while the blue cluster represents the supernatant. From the clusters obtained, it is possible to obtain an averaged spectrum for the coacervate phase and one for the supernatant phase (Figure 4). These spectra were used to obtain the polymer and

Research Article
doi.org/10.1002/cmtd.202500005

Chemistry Europe
European Chemical Societies Publishing

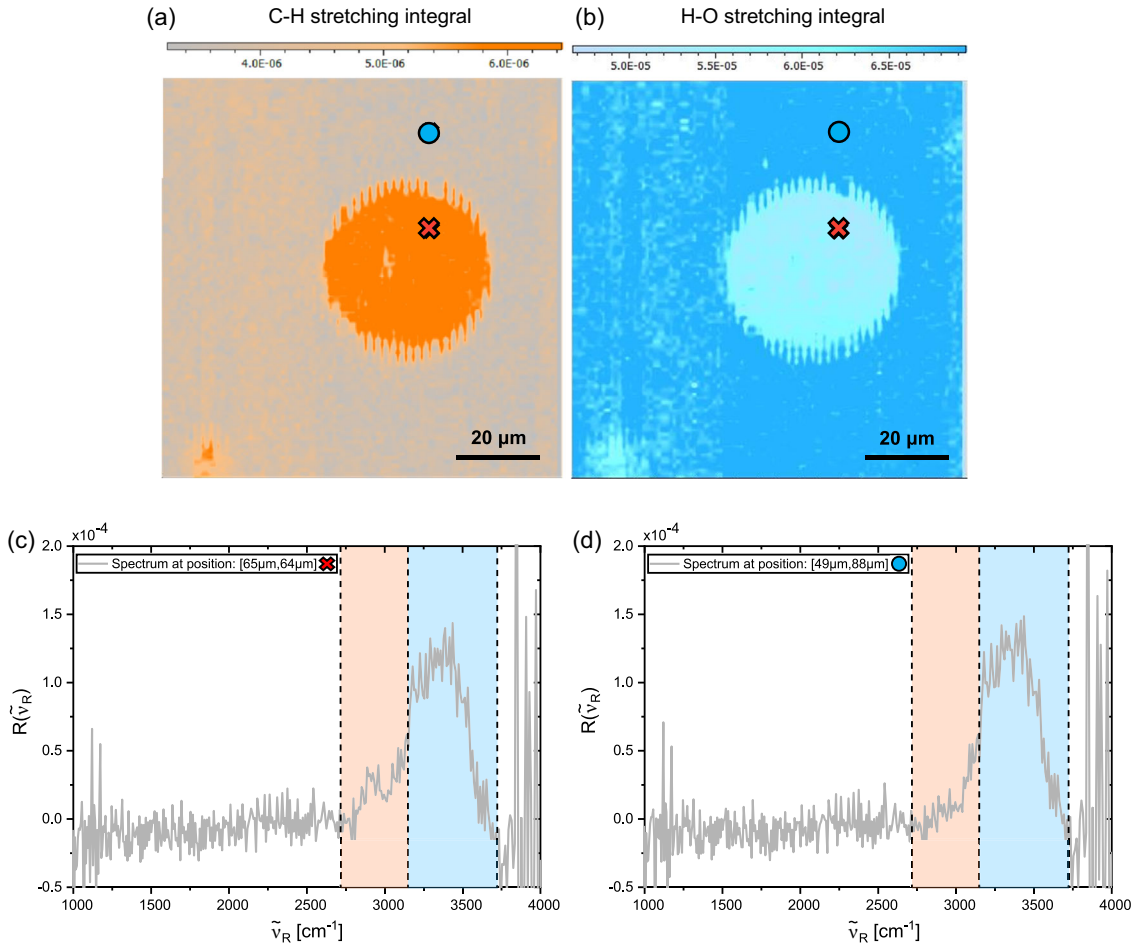

Figure 3. Chemical maps of the partitioning of the coacervate samples forming components. Chemical maps of the distribution of a) polymer and b) water in the coacervate and supernatant phase for a $c_t^{polymer} = 0.039$ M and $c_t^{KBr} = 1.58$ M coacervate sample. The maps were obtained by univariate analyses using the spectrally integrated area indicated in spectra c) and d). Polymer contribution is highlighted in orange, while that of water is in blue. The crosses and circles mark the location of which Raman spectra are depicted.

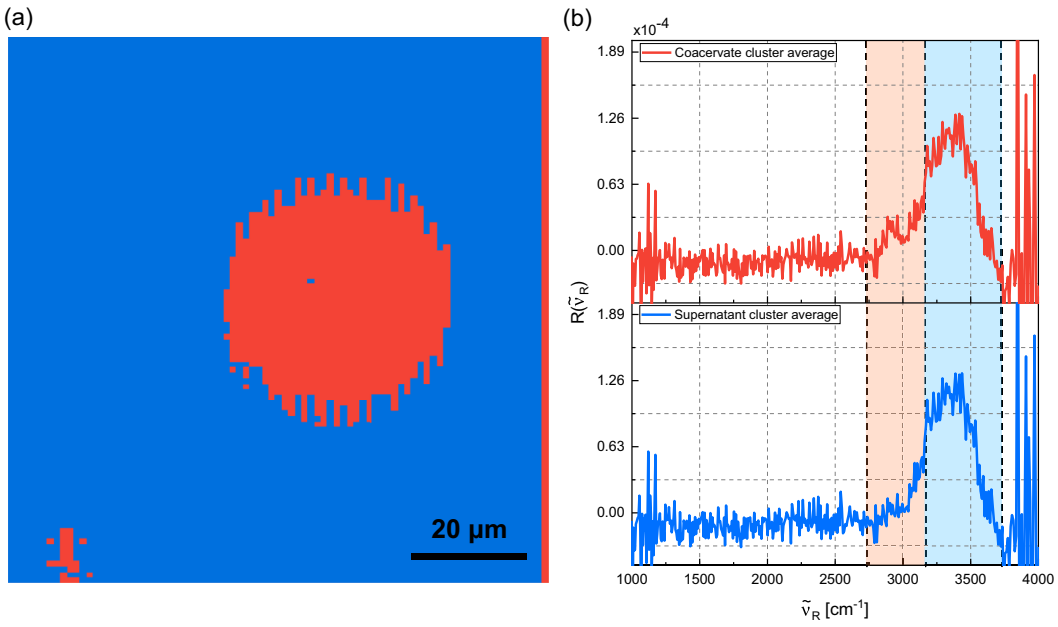

Figure 4. Chemical map a) obtained from the measurements depicted in Figure 3 via hierarchical cluster analysis, and the averaged spectra b) obtained from each cluster.

water concentration in the supernatant and coacervate phase. A Gaussian deconvolution was used to separate the contributions of the polymer and water in the spectra (Figure S1, Supporting Information). The water concentration in the supernatant phase was considered to be equal to the one of neat water $c_s^{water} = 55.56$ M (concentration of pure water, using $M_{water} = 18\ g\ mol^{-1}$). This value is used to determine the water concentration inside the coacervate phase. For the coacervate phase, the polymer concentration obtained was $c_c^{polymer} = 0.37 \pm 0.04$ M and the water concentration $c_c^{water} = 52.9 \pm 0.8$ M. The polymer concentration in the supernatant $c_s^{polymer}$ was below the detection limit of ≈0.1 M.

Additional FSRM measurements were conducted on coacervate samples obtained with varying c_t^{KBr} concentrations. The salt concentrations used were $c_t^{KBr} = 1.50$, 1.54, and 1.64 M, with the total polymer concertation $c_t^{polymer} = 0.039$ M kept constant. All Raman datasets obtained were treated in the same fashion as described above. The corresponding uni- and multivariate chemical maps, as well as the cluster spectra for the other total salt concentrations, can be found in the Supporting Information (Figure S2–S4, Supporting Information). **Figure 5** depicts the polymer $c_c^{polymer}$ and water c_c^{water} concentrations inside the coacervate phase for these samples. The decrease in the polymer concentration $c_c^{polymer}$ with salt addition is in line with previous reports.[19,20,53]

Thus, with FSRM, one may determine polymer and water concentrations for coacervate-forming samples relying on minute amounts. Yet, since KBr dissociates in water into monoatomic ions which are not Raman active, a key characteristic of complex

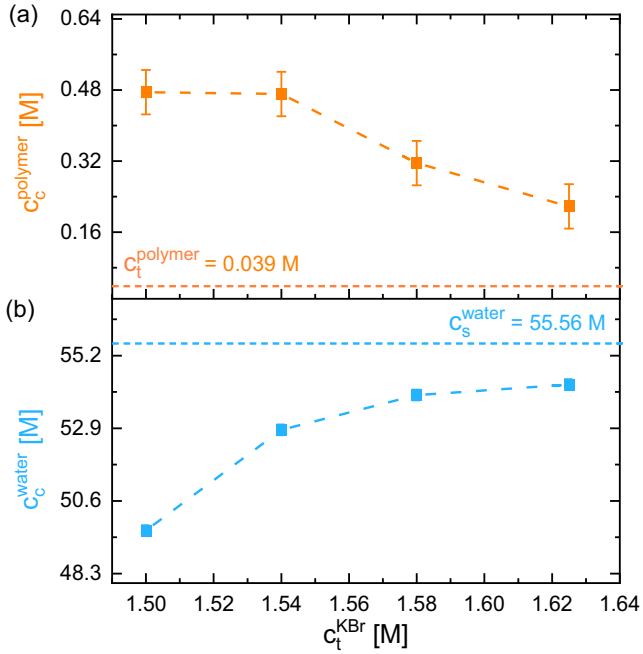

Figure 5. Concentration of polymer and water in the coacervate phase for the KBr coacervate samples. The concentrations $c_c^{polymer}$ a) and c_c^{water} b) obtained are plotted as a function of the concentration c_t^{KBr}. The concentrations were derived from averaged cluster analysis spectra as depicted in Figure 4. The orange horizontal line in a) indicates the total polymer concentration $c_t^{polymer}$ used to obtain the coacervate samples, and the blue horizontal line in b) indicates the water concentration in the supernatant phase c_s^{water}.

coacervates is missing so far: the salt concentrations c_c^{salt} and c_s^{salt}. To address this issue, the Raman-active salt NH_4SCN was used to determine the salt concentration in both the coacervate and supernatant phases. Phase separation was successfully achieved for PDADMAC-PSS samples using NH_4SCN. This was achieved for a constant total polymer concentration of $c_t^{polymer} = 0.014$ M, with the total NH_4SCN concentration ranging from 1.15 to 1.51 M. As for the KBr samples, datasets were first analyzed univariately. For the water and polymer contents, the same spectral ranges were used (**Figure 6**d,e). For the NH_4SCN content, the region around 2064 cm^{-1} (SCN^- stretching region) was integrated.

The chemical maps obtained for the NH_4SCN samples indicate the polymer (Figure 6a) and water (Figure 6b) partitioning as already observed for the KBr samples. However, it is now possible to observe the salt partitioning between the coacervate and supernatant phase as well (Figure 6c). This can be illustrated by two representative Raman spectra, one recorded for a position within the coacervate droplet (Figure 6d) and the other one outside (Figure 6e). The SCN^- signal is by a factor of 1.22 times higher inside than outside the droplet.

Regarding the droplet diameter, the value obtained was ≈53.7 μm for the C—H stretching map, ≈54.3 μm for the O—H stretching map, and ≈53.2 μm for the SCN^- stretching map. Again, the coacervate droplets have similar sizes in all three chemical maps, indicating that the identification of the coacervate and supernatant phases can be achieved using any of the three parameters (C—H, O—H, and CN^- stretching modes). In the image of the coacervate droplet, the presence of a hole within the droplet may be attributed to the dynamics of its formation. Specifically, this hole could have formed during the coalescence process of smaller precursor droplets. Hierarchical cluster analysis was also performed on this Raman dataset. The spectral regions used in the cluster analysis are the same as those used to obtain the univariate chemical maps (highlighted in Figure 6d,e). The respective chemical map is shown in **Figure 7**a, together with the average spectra for each cluster (b).

As for the KBr samples, coacervate and supernatant phases can be clearly discriminated based on this analysis. The average Raman spectra reveal that water and NH_4SCN are present in both phases, albeit in different concentrations. Polymer is only detected in the coacervate droplet. With the same procedure as used for the KBr samples, polymer and water concentrations were derived from the averaged spectra. The NH_4SCN concentration was determined by performing a Gaussian fit on the SCN^- peak and using a calibration curve (Figure S5, Supporting Information). Here, the concentration of NH_4^+ in both the coacervate and supernatant phases is assumed to be identical to the measured value for SCN^- as required by charge balance. Note that the salt concentration $c_t^{NH_4SCN}$ is much higher than the polymer concentration $c_t^{polymer}$. Thus, the counterions of the polyelectrolytes (Na^+ and Cl^-) play little role in charge balance. The polymer and water concentration obtained for the $c_t^{NH_4SCN} = 1.21$ M coacervate sample in the coacervate phase are $c_c^{polymer} = 0.65 \pm 0.05$ M and $c_c^{water} = 51.1 \pm 0.2$ M, respectively. For the NH_4SCN concentration, the value obtained in the coacervate phase was $c_c^{NH_4SCN} = 1.36 \pm 0.03$ M and in the supernatant phase $c_s^{NH_4SCN} = 1.13 \pm 0.03$ M. Thus, the NH_4SCN concentration is higher

Research Article
doi.org/10.1002/cmtd.202500005

Chemistry Europe
European Chemical Societies Publishing

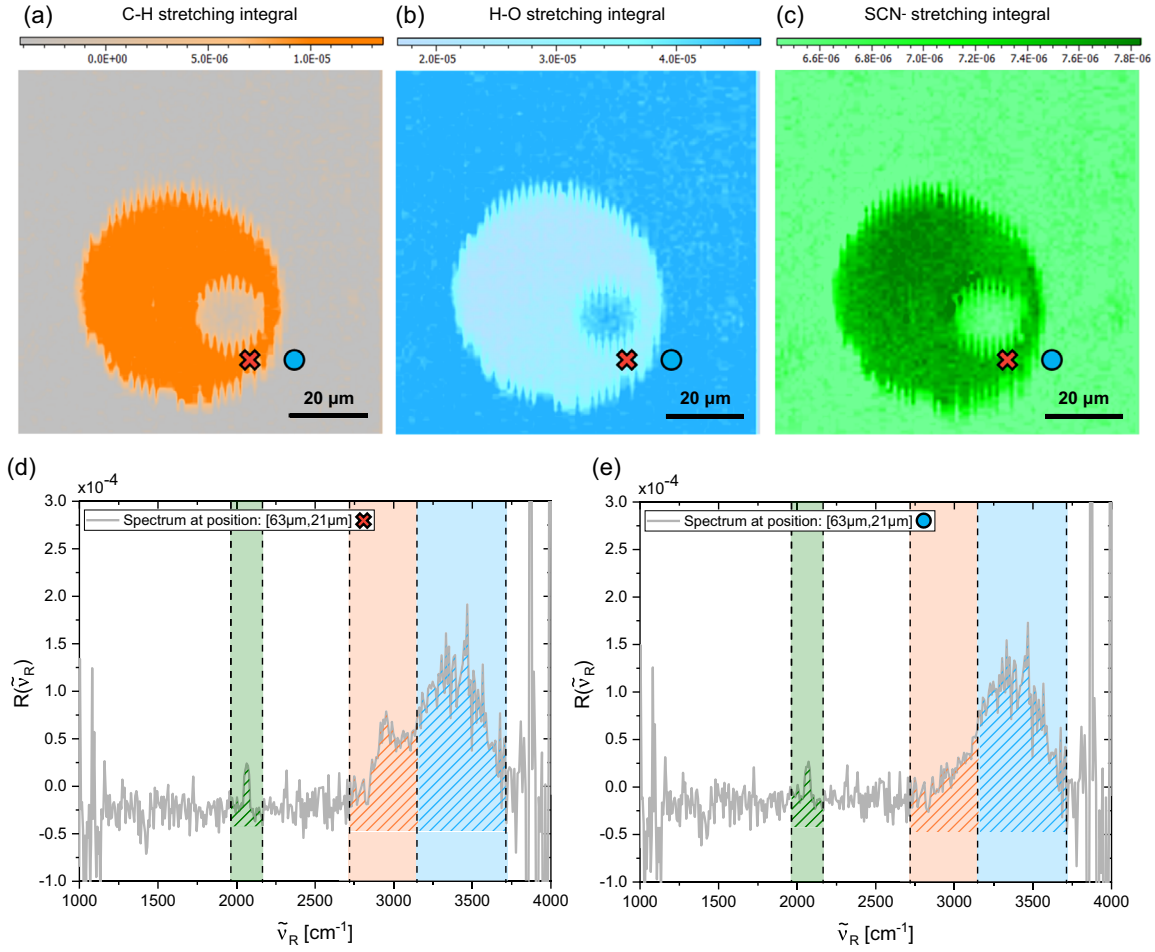

Figure 6. Chemical maps of the distribution of a) polymer, b) water, and c) SCN^- in the coacervate and supernatant phase for a $c_t^{polymer} = 0.014$ M and $c_t^{NH_4SCN} = 1.21$ M coacervate sample. The maps were obtained by univariate analysis using the spectral integrals indicated in spectra d) and e). Polymer contribution is highlighted in orange, water in blue, and SCN^- in green. The crosses and circles mark the location at which the Raman spectra (d) and (e) were recorded.

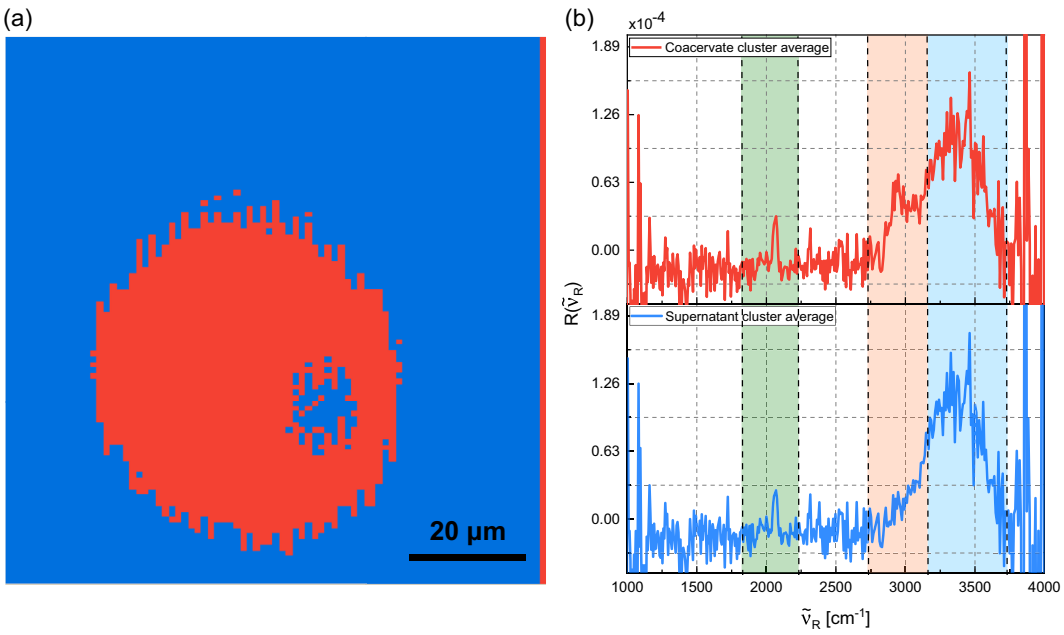

Figure 7. Chemical map a) obtained from the measurements depicted in Figure 6 via hierarchical cluster analysis, and the averaged spectra b) obtained from each cluster.

by a factor of 1.20 ± 0.04 in average in the coacervate droplet compared to the supernatant. This value is in the same range as the enrichment value mentioned above, of 1.22, which resulted from the comparison of one Raman spectrum in each phase. The enrichment value of 1.20 ± 0.04 was derived from an average over all spectra in the two phases; it is, thus, statistically more reliable.

The NH_4SCN enrichment deduced from the Raman measurements rests on an important assumption. FSRM signals depend not only on the concentrations but also on the Raman cross sections. Therefore, the observed Raman signal levels for NH_4SCN in the two phases could also be explained with identical concentrations and different cross sections. To exclude this effect, or at least to render it unlikely, the Raman results on the NH_4SCN partitioning were crosschecked by IR spectroscopy. As no IR microscope was at hand, coacervate samples were characterized after macroscopic phase separation, that is, not on coacervate droplets dispersed in the supernatant. The drawback of using macroscopic phase separation is the requirement for a substantial amount of material. Measuring the water content in each phase using IR spectroscopy was not possible due to the high IR absorption of water, which saturated the spectrometer. This issue persisted despite the sample thickness being only 25 μm.

IR spectra for the separated coacervate and supernatant phases are shown in **Figure 8**. The IR peaks at ≈1454, 2064, and 2874 cm^{-1} are attributed to the bending mode of NH_4^+, the stretching mode of SCN^-, and the stretching mode of NH_4^+, respectively.[49,54] In the coacervate IR spectrum, in addition to the NH_4SCN IR peaks, there are peaks at 1035 and 1185 cm^{-1} attributed to symmetric and antisymmetric stretching vibrations of the SO_3^- group and a peak at 1129 cm^{-1} attributed to the in-plane skeletal vibration of the benzene ring, all from the PSS polymer.[55] There is also one peak at 1475 cm^{-1}, overlapping with the NH_4^+ peak, assigned to the CH_3 bending vibrations of PDADMAC.[56] It is also possible to observe the polyelectrolytes' C—H stretching modes appearing in the broadband peak at ≈2874 cm^{-1}.

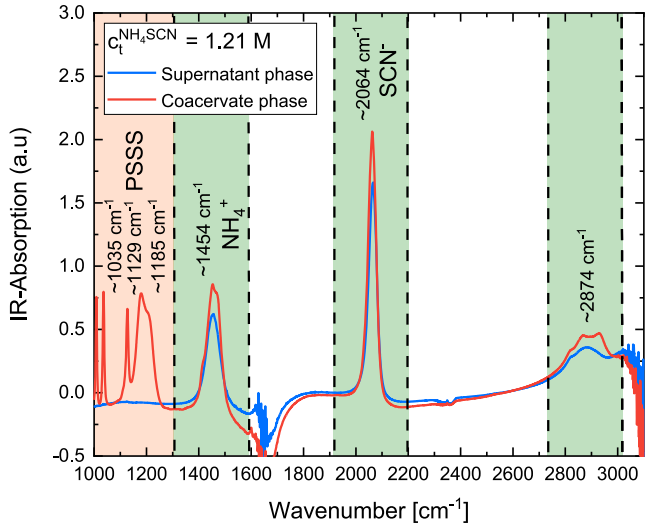

Figure 8. IR absorption spectra of the coacervate and the supernatant phases of a $c_t^{polymer} = 0.014$ M and $c_t^{NH_4SCN} = 1.21$ M sample.

The salt and polymers partitioning for the separated coacervate and supernatant phases deduced from the IR spectra exhibits the same trends as seen in the Raman measurements. The IR peaks related to the NH_4SCN salt are higher in the coacervate phase compared to the peaks obtained for the supernatant phase. Based on this observation, the assumption that the different Raman signals in the two phases originate from different Raman cross sections seems unlikely. As in the Raman measurements, in the IR spectra of the supernatant phase, the signals of the polyelectrolytes PDADMAC and PSS are below the detection limit. To determine the concentrations of polymer and NH_4SCN in the coacervate and supernatant phases using IR measurements, a Voigt deconvolution was applied to the peaks assigned to the polymer and salt (Figure S6, Supporting Information). The polymer concentration was determined using a PSS calibration measurement. The NH_4SCN concentration was derived by averaging the NH_4^+ and SCN^- contribution and using a calibration curve (Figure S7, Supporting Information). The calculated concentrations of NH_4^+ and SCN^- in each spectrum were effectively identical within experimental uncertainty. This supports the assumption that equivalent amounts of $NH4^+$ and SCN^- are present in each phase.

To obtain a phase diagram for the NH_4SCN coacervate samples, additional FSRM measurements were conducted on coacervate samples with different total NH_4SCN concentrations. Besides the $c_t^{NH_4SCN} = 1.21$ M sample, three more NH_4SCN concentrations were studied: $c_t^{NH_4SCN} = 1.25$, 1.35, and 1.40 M. All samples were prepared with a constant total polymer concentration $c_t^{polymer} = 0.014$ M, and the uni- and multivariate chemical maps, as well as the cluster spectra, can be found in the Supporting Information (Figure S8–S11, Supporting Information). With IR spectroscopy, coacervate samples with total NH_4SCN concentrations $c_t^{NH_4SCN} = 1.21$ and $c_t^{NH_4SCN} = 1.40$ M were studied, both with a constant total polymer concentration $c_t^{polymer} = 0.014$ M. These measurements can also be found in the Supporting Information (Figure S12–S13, Supporting Information).

The polymer concentration for the coacervate phases (**Figure 9**a), obtained from the Raman and IR measurements performed on the NH_4SCN samples, decreases with increasing concentration $c_t^{NH_4SCN}$. The IR measurements reveal a somewhat higher concentration $c_c^{polymer}$, of about 1.3 times for the $c_t^{NH_4SCN} = 1.21$ sample and 1.4 times for the $c_t^{NH_4SCN} = 1.40$ sample.

Although polymer concentration $c_c^{polymer}$ derived from Raman and IR measurements differs, the fractional change with total salt concentration is virtually identical. The polymer concentration $c_c^{polymer}$ decreases by a factor of ≈0.6 for both IR and Raman measurements when comparing the value obtained for the $c_t^{NH_4SCN} = 1.21$ and 1.40 M samples. As the water signal saturates in the IR measurements, the water concentration was only determined by FSRM.

The concentrations $c_c^{NH_4SCN}$ and $c_s^{NH_4SCN}$, together with the concentration $c_c^{polymer}$, obtained from Raman and IR measurements were used to construct a phase diagram for the coacervation of NH_4SCN samples (**Figure 10**). In this diagram, data points representing the composition of the supernatant are plotted in blue, and those for the coacervates are in red. Tie lines connect phases

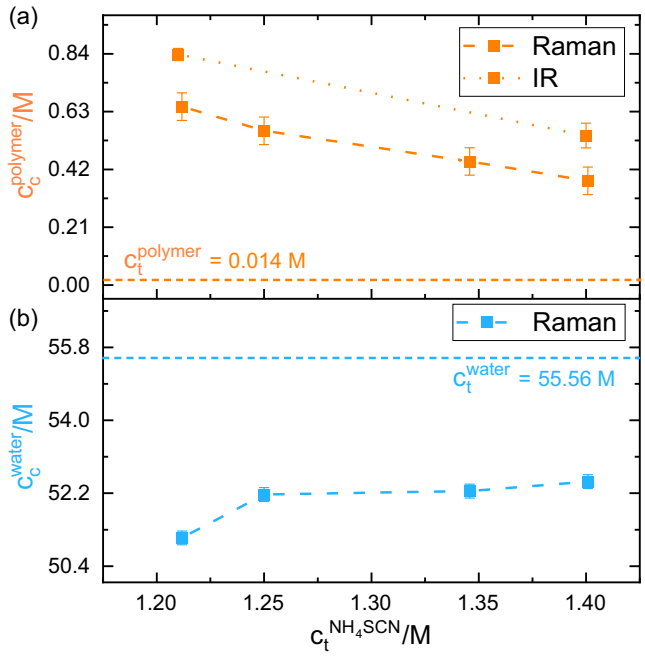

Figure 9. Concentration of polymer and water in the coacervate phase for the NH_4SCN coacervate samples. The concentrations $c_c^{polymer}$ a) and c_c^{water} b) obtained are plotted as a function of the total salt concentration $c_t^{NH_4SCN}$. The concentrations based on FSRM were derived from a cluster analysis as depicted in Figure 7. The values for the concentrations $c_c^{polymer}$ and c_c^{water} for total salt concentration $c_t^{NH_4SCN} = 1.40$ M were obtained from the average of three different measurements. These measurements were used to obtain the error bars for the FSRM measurements as discussed in the Experimental Section. The three chemical maps, and cluster spectra can be seen in the Supporting Information (Figure, Supporting Information). The orange horizontal line in (a) indicates the total polymer concentration $c_t^{polymer}$ used to obtain the coacervate samples, and the blue horizontal line in (b) indicates the water concentration in the supernatant phase c_s^{water}.

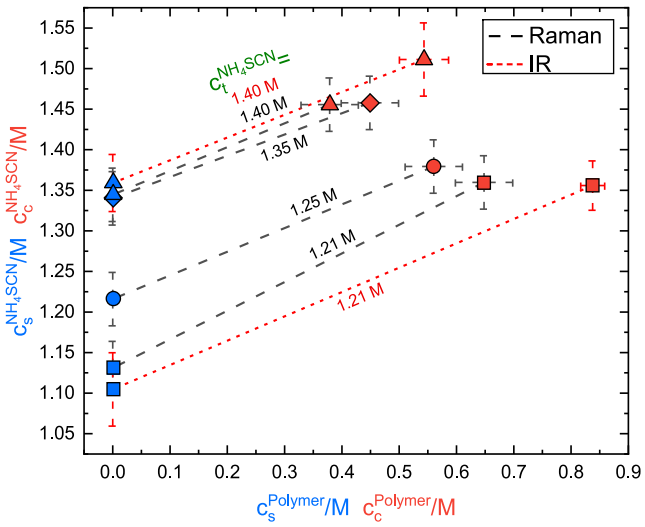

Figure 10. Phase diagram of the partitioning of polymers and salt in the coacervate and supernatant phases, obtained by FSRM and IR measurements. The blue symbols represent the concentrations $c_s^{polymer}$ and $c_s^{NH_4SCN}$ in the supernatant phase, and the red symbols represent the concentrations $c_c^{polymer}$ and $c_c^{NH_4SCN}$ in the coacervate phase. The tie lines (dashed) connect phases in equilibrium obtained for the same sample. On the top of the lines, the $c_t^{NH_4SCN}$ of each sample is represented. The values of concentrations $c_{c-s}^{polymers}$ and $c_{c-s}^{NH_4SCN}$ for the total salt concentration $c_t^{NH_4SCN} = 1.40$ M were obtained from the average of three different measurements.

in equilibrium with each other. Their upward slopes indicate the enrichment of NH_4SCN in the coacervates addressed above. This enrichment is similar for both Raman and IR measurements. For the $c_t^{NH_4SCN} = 1.21$ M sample measured with Raman, the salt concentration in the coacervate phase is higher by a factor of 1.20 ± 0.03 compared to the supernatant phase. For the IR measurement, this enrichment is of 1.23 ± 0.04. For the $c_t^{NH_4SCN} = 1.40$ M samples, the salt enrichment factor is 1.08 ± 0.03 for the Raman measurements and 1.11 ± 0.03 for the IR measurements. It is also noteworthy that the uncertainty is similar for both Raman and IR measurements, but arising from different sources. With Raman, both phases were characterized relying on one sample, and error margins are mostly due to spectroscopic issues. For the IR determinations, phases had to be separated and measured individually. Attaining identical IR pathlengths (25 μm) for both phases proved challenging, and this contributed to the IR error margins.

3. Discussion

The central findings of this study may be summarized as follows: i) with FSRM, sample volumes of complex coacervates as small as 20 μL were characterized within a few minutes. The characterization yields the shape and sizes of coacervate droplets and can quantify polymer, water, and salt partitioning. The salt partitioning requires the utilization of a Raman-active salt, NH_4SCN in this study. ii) The polymer and water concentrations in the phases of PDADMAC/PSS complex coacervates were measured for two different salts, KBr and NH_4SCN. The results for KBr will be compared with literature values. iii) Raman and IR measurements diverged regarding the polymer concentration in the coacervate phase. iv) For the PDADMAC/PSS-NH_4SCN complex coacervate system, salt enrichment in the coacervate phase was found. These four topics will now be briefly discussed. i) To measure the polymer and/or salt concentration in coacervates or PECs, different analytical techniques have been used.[1,2,19–29] These approaches generally involve separating the supernatant and coacervate phases via centrifugation, which demands relatively large sample volumes that can range from 1.5 to 50 mL. In contrast, FSRM offers a standalone and label-free approach capable of characterizing coacervate samples using volumes as small as 20 μL, without the need for any prior sample preparation. Moreover, the measurements are conducted relatively quickly, within 17 min, enabling the simultaneous analysis of both the coacervate and supernatant phases. This is particularly advantageous given the dynamic nature of coacervates and their tendency to coalesce. Higher acquisition speeds and fluorescence rejection are the advantages of FSRM over conventional Raman microscopy. With the latter technique, in principle, the same results could be obtained albeit with much longer acquisition times. A balanced comparison of the two Raman approaches also has to consider the SNR. We are not aware of any characterization of PDADMAC/PSS coacervates using conventional Raman microscopy. We, thus, use a study by Choi et al.[35] where conventional Raman microscopy was used to investigate the formation of LLPS protein droplets.

While the SNR was not explicitly reported in their publication, it can be estimated by calculating the ratio between a Raman band strength and the noise level, approximated by the baseline fluctuations. For comparison, the water signal was used, as it is present in samples studied by both techniques. The SNR_{FSRM} for the water band in the Figure 3d spectra is ≈14.5 for an acquisition time of 0.1 s. For a micro-Raman spectrum of pure tris-buffered solution, the calculated SNR_{MR} for the water band was estimated to be ≈53 for an averaging time of 25 s. Assuming that SNR scales with the acquisition time (t) by SNR $\sim\frac{1}{\sqrt{t}}$,[57] the estimated SNR_{MR} for an acquisition time of 0.1 s is of ≈3.4. Since the conventional Raman microscope used by Choi et al. was a commercial system, this comparison is likely representative for other conventional Raman microscopes as well.

These findings indicate that FSRM offers significant advantages for generating chemical maps of LLPS samples, drastically reducing acquisition time per spectrum. Also, since FSRM allows for shorter acquisition time, it may enable the real-time monitoring of dynamic processes involving phase separation. Concerning the salt partitioning, a drawback of all Raman techniques is that salts consisting of molecular ions are required. Salts like NaCl and KBr, commonly used in coacervation studies,[1,20,21,33,48,53] cannot be considered. Yet, the use of molecular salts still gives valuable insights and sufficient variability in ion properties. For example, in studies on the impact of salt properties on coacervation, a "fine-tuning" of ion size, valency, kosmotropy/chaotropy, and pH dependencies is possible for molecular ions. We also note that molecular ions play an important role in biology. For instance, the concentration in blood plasma of the ion HCO_3^- (which is typically around 23 mM[58]) is on the same magnitude as the one of Cl^- (typically around 70 mM[59]). ii) The phase diagrams of PDADMAC/PSS coacervate systems in the presence of KBr were previously reported by Liu et al.,[19] Radhakrishna et al.[20] and Wang et al.[25] These studies report a similar trend. The polymer concentration in the coacervate phase $c_c^{polymer}$ decreases as the total salt concentration c_t^{salt} increases, which aligns with the findings reported here. Also, in absolute terms, the polymer concentrations $c_c^{polymer}$ compare rather favorably with previous reports[19,20] for similar salt concentrations. In the present study, polymer concentration is reported as pairs of repeat units. In some of these studies (namely Liu et al.[19] and Radhakrishna et al.[20]), the concentrations of the repeat units of the polycations and polyanions were added; therefore, to arrive at the concentrations used here, the values reported in these articles were divided by two. For salt concentrations similar to ours ($c_t^{salt} \approx 1.5$ M), Liu et al.[19] report polymer concentrations in the coacervate phase $c_c^{polymer}$ of around 0.4 M. In Radhakrishna et al.,[20] polymer concentrations $c_c^{polymer}$ of ≈0.7 M were measured. In the study by Wang et al.,[25] polymer concentrations $c_c^{polymer}$ of ≈0.8 M were determined. Thus, there is quite a variance in the published values. Our polymer concentration $c_c^{polymer}$ (0.48 M) for a salt concentration c_t^{salt} of 1.5 M is within the range of these values. To the best of our knowledge, a phase diagram for the PDADMAC/PSS-NH_4SCN complex coacervate system was not yet reported in the literature. iii) For the NH_4SCN coacervate samples, the measured polymer concentration in the coacervate phase $c_c^{polymer}$ ranged from 0.38 ± 0.05 to 0.65 ± 0.05 M for the samples measured with Raman and 0.54 ± 0.05 M to 0.84 ± 0.02 for the samples measured with IR. The different conditions of the samples investigated—droplets dispersed in the supernatant for FSRM as opposed to bulk phase separation for IR—are most likely not responsible for the difference. Thermodynamics and kinetics discard this, as the following arguments illustrate. Concerning thermodynamics, the enrichment factor can be related with the difference in chemical potential for a reference condition between the two phases (Equation (2)),[60]

$$\mu_c^{polymer,0} - \mu_s^{polymer,0} = -RT\ln\frac{c_c^{polymer}}{c_s^{polymer}} \quad (2)$$

Here, R is the gas constant, and the temperature T was assumed to be 293 K. The ratio $\frac{c_c^{polymer}}{c_s^{polymer}}$ of the two concentrations is very high since the polymer concentration in the supernatant phase is very small and could not be determined here. No polymer signal was observed in the supernatant phase in either the Raman or IR measurements. Since the IR measurements have a better SNR, they can be used to determine the limit of detection and, consequently, the maximum possible polymer concentration in the supernatant. Using the spectra in Figure 7 and the corresponding polymer peak, the lowest detectable concentration is estimated to be ≈1 mM. Therefore, a value of 0.9 mM will be used for the calculations here. This upper boundary magnitude aligns well with the value reported by Liu et al.[19] who observed a polymer concentration of ≈5 mM in the supernatant phase for PDADMAC/PSS–KBr coacervates. Inserting these values yield a difference $\mu_c^{polymer,0} - \mu_s^{polymer,0}$ of the order of -10^4 J mol^{-1}. For the coacervate droplets dispersed in the supernatant (condition investigated by FSRM), the molar interfacial free energy $\overline{G}_\gamma$ contributes to the balance of Gibbs free energies.[60] A crude estimate shows that its contribution may be neglected here. The molar free energy $\overline{G}_\gamma$ is estimated via Equation (3),

$$\overline{G}_\gamma = \frac{\gamma A}{c_{water} V} = \frac{3\gamma}{c_{water} r} \quad (3)$$

The interfacial tension γ for coacervates amounts to ≈100 μN m^{-1},[61] which is small in comparison, for example, to oil in water (24–26 mN m^{-1}).[62] Multiplying this tension with the surface area A of a droplet yields a free energy which can be converted into a molar quantity by dividing the amount of substance in the droplet ($c_{water}V$). For simplicity, it is assumed that the droplet contains only water. The amount of substance is then given by the product of the water concentration and the volume of a droplet, $c_{water}V$. According to the Raman images, typical droplet radii are of the order of 10 μm. With these inputs, a molar free energy $\overline{G}_\gamma$ of ≈0.5 J mol^{-1} is estimated, which is five orders of magnitude smaller than the above difference of chemical potentials. Surface effects may, thus, be neglected here.

Concerning kinetics, it seems reasonable to assume that, for both conditions, polymer partitioning has equilibrated. Provided that the kinetics of the equilibrium is governed by diffusion, a simple consideration supports this. Of the two polyelectrolytes

used here, PDADMAC has the higher molecular mass and is thereby expected to limit the diffusion process. The diffusion coefficient D of PDADMAC (with Mw = 400–500 kg mol^{-1}) in a water-salt medium is in the order of 10^{-8} cm^2 s^{-1}.[63] This implies that PDADMAC passes through a droplet with a radius of 10 μm within ≈17 s. The PDADMAC sample used in this work has a Mw = 200–350 kg mol^{-1}, and therefore, an even faster diffusion is expected. Preparing and measuring these samples obviously takes much longer, and equilibrium may be assumed. Thus, the slight differences between FSRM and IR results have to be attributed to instrumental and/or spectroscopic effects. We can, for instance, not exclude that Raman and IR cross sections are affected slightly differently by the environment of the polymers in the coacervate phase. This difference aside, both techniques indicate a similar polymer enrichment in the coacervate phase by a factor of 40–60 with respect to the total concentration $c_t^{polymer}$. This enrichment is in line with the small volume fraction ϕ_c of ≈0.05 of the coacervate phase (see Equation (3)). iv) For NH_4SCN coacervate samples, salt was found to be enriched in the coacervate phase. In the literature studies for PDADMAC/PSS-KBr coacervate samples, a depletion of salt in the coacervate phase was observed.[19–21,24] As our approach is "blind" with respect to KBr, we cannot validate these findings. It was already shown by radiolabeling experiments that SCN^- ions have a higher enrichment factor in PECs consisting of PDADMAC/PSS then Br^- ions.[28] This factor may explain the higher concentration of SCN^- ions in the coacervate phase observed here. Since the enrichment of salt in PECs strongly depends on specific polyelectrolyte–ion interactions, having a tool that directly assesses salt partitioning regardless of the polyelectrolyte–ion pair being used is highly beneficial for characterizing coacervate systems.

4. Conclusion

FSRM was introduced in this study as a novel method for the characterization complex coacervates. Uni- and multivariate chemical maps were obtained depicting the coacervate droplets and the surrounding supernatant. The polymer, water, and salt partitioning between the coacervate and supernatant phases was characterized, therefore fully describing all components controlling LLPS for complex coacervate samples. A phase diagram for the PDADMAC/PSS-NH_4SCN coacervate samples was obtained depicting salt enrichment in the coacervate phase. FSRM enables simultaneous and fast quantitative and qualitative analyses of both coacervate droplets and the supernatant phase using only a small amount of sample.

5. Experimental Section

FSRM

The FSRM instrument was detailed before;[47,64,65] here, only the pertinent parameters were summarized. The measurements were performed by focusing the probe and pump beam onto the sample, with average laser powers of 1.5 and 16 mW, respectively. In FSRM, Raman spectra are derived from the probe spectra in presence ($S_{probe+pump}$) and in the absence (S_{probe}) of the pump light. The technique is based on femtosecond stimulated Raman spectroscopy,[66] where photons in the probe beam (wavenumber $\tilde{\nu}_{probe}$) are annihilated (stimulated Raman loss), while photons in the pump beam (wavenumber $\tilde{\nu}_{pump} < \tilde{\nu}_{probe}$) are generated (stimulated Raman gain), if the Raman shift $\tilde{\nu}_R$ (Equation (4))

$$\tilde{\nu}_R = \tilde{\nu}_{probe} - \tilde{\nu}_{pump} \tag{4}$$

matches a Raman resonance of the sample. Stimulated Raman spectra $R(\tilde{\nu}_R)$ versus $\tilde{\nu}_R$ were derived from the spectra $S_{probe}(\tilde{\nu}_R)$ and $S_{probe+pump}(\tilde{\nu}_R)$ via Equation (5)

$$R(\tilde{\nu}_R) = 1 - \frac{S_{probe+pump}(\tilde{\nu}_R)}{S_{probe}(\tilde{\nu}_R)} \tag{5}$$

Note that $R(\tilde{\nu}_R)$ is dimensionless and obeyed $0 \leq R(\tilde{\nu}_R) \leq 1$.

The coacervate samples were scanned with a piezo stage, and the total time to record a $100 \times 100\ \mu m^2$ Raman dataset, scanning in steps of ≈1 μm, was about 17 min.

FTIR

FTIR was used to obtain IR absorption spectra of the coacervate and supernatant phases of coacervate samples. The measurements were carried out using an FTIR spectrometer Vertex 80 V from Bruker. The light source used was a SiC Globar (1500 K), and the detector used was a DigiTect DLaTGS pyroelectric detector. A sample cell with CaF_2 windows (Crystal GmbH) separated by a 25 μm spacer was used. For each spectrum, 128 scans were averaged. The total acquisition time was ≈7 min. The solvent background was corrected for by recording IR spectra of the sample cell filled with water.

Sample Preparation

The polyelectrolytes PDADMAC and PSS used in this study were purchased from Sigma-Aldrich, with molecular weights (M_W) of 200 000–350 000 g mol^{-1} and 70 000 g mol^{-1}, respectively. KBr (potassium bromide) was purchased from Thermo Fisher Scientific (laboratory reagent grade, ≥99%), and NH_4SCN (ammonium thiocyanate) was purchased from Carl Roth (p.a., ACS, ISO ≥99%)). Deionized water was used to prepare the solutions for LLPS. In the preparation of the polymer solutions, care was taken to ensure that for each cationic repeat unit of PDADMAC there is an anionic repeat unit in PSS. Hereby, the molecular masses of the respective repeat units were considered (including counter ions).

To prepare the solutions for LLPS, stock solutions of each component were initially compounded. Both PDADMAC and PSS stock solutions with a concentration of 0.45 M, referring to the repeat units, were prepared. For the salts, stock solutions with concentrations of 2.5 M for KBr and 3.0 M for NH_4SCN were prepared. Samples for LLPS were obtained as follows: first, the salt solution (KBr or NH_4SCN) was added to a tube; then, the PSS solution was added, and the solution was agitated for about 10 s until homogeneity. Next, a volume of the PDADMAC solution identical to the one of the PSS solution was added. Finally, deionized water was added to achieve the intended final concentration for each component in the sample. The formation of LLPS was indicated by the transition of the sample from a clear solution to a turbid mixture. The different coacervate samples studied were prepared to have a constant total polymer concentration, while varying the total salt concentration. For the KBr coacervate samples, the total polymer concentration was 0.039 M with the total salt concentration ranging from 1.50 to 1.63 M. For the NH_4SCN samples, the

total polymer concentration was 0.014 M with the total salt concentration ranging from 1.21 to 1.40 M.

The phase partitioning of components in the coacervate samples was investigated using FSRM and FTIR. For the coacervate samples investigated by FSRM, the samples were agitated before the measurements to avoid large clusters of droplets. The measurements were performed on microscopy slides equipped with a 20 μL well. The well was created by adhesive films with indentations (Carl Roth, AXC3.1) glued to the microscopy slides. The well on the microscopy slide was then filled up with the sample and covered afterwards with another microscopy slide to avoid contamination during the measurement. The sample was sealed with clear nail polish and placed on the scanning stage of the FSRM instrument. A coacervate droplet was subsequently discerned within the sample and scanned, alongside the surrounding supernatant. For the IR measurements, it was necessary to first separate the coacervate phase from the supernatant phase: this was achieved by preparing a 12 mL coacervate sample. In this manner, a sufficiently large coacervate phase is obtained for the measurement. The sample was allowed to rest for 2 days to ensure complete separation of both phases. The coacervate and supernatant phases were then separated and measured individually. The measurements were performed using a cuvette with CaF_2 windows and a path length of 25 μm.

Data Analysis

The Raman datasets obtained from the FSRM measurements were converted into chemical maps using uni- and multivariate analysis using the Epina ImageLab software. First, a maximum noise fraction (MNF) transformation algorithm, embedded in the software, was used on the dataset. The MNF technique is similar to principal component analysis and was used to enhance the SNR, thus enhancing image quality.[67] Afterwards, univariate and multivariate analysis was performed to generate maps of the distributions of polymer, salt, and water ("chemical maps"). For the univariate analysis, spectral ranges in the Raman spectra characteristic of each compound were identified. False color images visualizing the integrals covering these ranges were then generated. In the multivariate analysis, the integrals were considered simultaneously. A hierarchical cluster analysis algorithm,[68] as implemented in the Epina ImageLab software, was used. The algorithm groups spectra into clusters based on similarities for the chosen spectral ranges. By grouping spectra with similar polymer, water, and salt concentrations into clusters, it was possible to simultaneously consider all important spectral parameters to identify the coacervate and supernatant phases.

From the clusters obtained, an averaged spectrum for each cluster was calculated and used to quantify the amount of polymer, water, and salt present in each phase. For the polymer and water concentrations, a Gaussian deconvolution was applied to assign polymer and water Raman peaks in the averaged cluster spectra. The water peak around ≈3400 cm^{-1} of the cluster spectrum for the supernatant was used to scale all cluster spectra. The water signal of the supernatant essentially did not change with the composition.

Using Raman spectra represented by these Gaussians, the polymers' concentration was derived. Here, Raman signals of polymer solutions (not LLPS) with defined characteristics were used for the calibration. The approach made use of the linear scaling of the SRS signal with concentration.[69] The SCN^- concentration of NH_4SCN for each phase was determined by performing a Gaussian fit on the Raman band assigned to SCN^- stretching mode in the averaged cluster spectra. For the conversion of the Raman signal into NH_4SCN concentration, a calibration curve was recorded.

To quantify the uncertainty of the FSRM measurements, three different measurements of samples with $= 1.40$ M and $c_t^{polymer} = 0.014$ M concentrations were performed. Two of these measurements were recorded on the same sample after an interval of ≈20 min. The third measurement was performed on a different sample with identical total polymer and salt concentrations. Therefore, both uncertainties rising from the measurement procedure and the sample preparation were considered. The error bars shown for the polymer, water, and salt concentrations in all the FSRM diagrams represented the standard deviation of the mean of these three measurements.

The quantification of the polymer and NH_4SCN content in samples analyzed via FTIR followed a similar protocol. Peaks assigned to the polymer and salt were fitted using a Voigt profile, and the fitted areas were utilized to calculate the concentrations. Polymer concentrations were determined by comparing the fitted area obtained from the coacervate sample spectra with the Voigt-fitted areas derived from a PSS solution (not LLPS) spectra of known concentration. More specifically, only the PSS peaks were considered in the polymer concentration calculation, since the PDADMAC peaks were comparatively small and overlap with the NH_4 peak. The salt concentration was determined by fitting the NH_4^+ and SCN^- peaks and averaging their contributions. The salt concentration was then obtained by using a calibration curve, also obtained from FTIR measurements of NH_4SCN samples with known concentrations.

Acknowledgements

We thank Michele Illmann (HHU, Düsseldorf) for help in producing the diagram in Figure 1 and Jan Martin Halada for preliminary tests concerning phase separation. S.S. acknowledges funding by the German Research Foundation (project number SCHM 2748/7-1).

Conflict of Interest

The authors declare no conflicts of interest.

Author Contributions

Francisco van Riel Neto: conceptualization (equal); data curation (lead); formal analysis (lead); investigation (lead); methodology (lead); visualization (lead); writing—original draft (lead). **Carolin Borbeck**: methodology (equal); visualization (equal); writing—review and editing (supporting). **Torben Henning Saatkamp**: formal analysis (supporting); investigation (supporting); methodology (supporting). **Maxine Kenny**: formal analysis (supporting); investigation (supporting); methodology (supporting). **Stephan Schmidt**: conceptualization (equal); writing—review and editing (equal). **Peter Gilch**: conceptualization (lead); supervision (lead); writing—review and editing (lead).

Data Availability Statement

The data that support the findings of this study are available from the corresponding author upon reasonable request.

Keywords: complex coacervates · non-linear Raman microscopy · phase diagram · polyelectrolytes · salt partitioning

[1] C. E. Sing, S. L. Perry, *Soft Matter* **2020**, *16*, 2885.
[2] S. P. Moulik, A. K. Rakshit, A. Pan, B. J. C. Naskar, *Colloids Interfaces* **2022**, *6*, 45.
[3] A. Baer, S. Hänsch, G. Mayer, M. J. Harrington, S. Schmidt, *Biomacromolecules* **2018**, *19*, 4034.
[4] M. D. Illmann, L. Schäfl, F. Drees, L. Hartmann, S. Schmidt, *Biomacromolecules* **2023**, *24*, 2532.
[5] N. A. Yewdall, A. A. André, T. Lu, E. J. C. O. Spruijt, *Curr. Opin. Colloid Interface Sci.* **2021**, *52*, 101416.
[6] M. Heim, D. Keerl, T. Scheibel, *Angew. Chem. Int. Ed.* **2009**, *48*, 3584.
[7] A. H. Hofman, I. A. van Hees, J. Yang, M. Kamperman, *Adv. Mater.* **2018**, *30*, 1704640.
[8] H. G. Hansma, Liquid–liquid phase separation at the origins of life. In *Droplets of Life*, San Diego, Academic Press **2023**, pp 251–268.
[9] A. Veis, C. Aranyi, *J. Phys. Chem.* **1960**, *64*, 1203.
[10] C. Schmitt, S. L. Turgeon, *Adv. Colloid Interface Sci.* **2011**, *167*, 63.
[11] A. M. Rumyantsev, N. E. Jackson, J. J. De Pablo, *Annu. Rev. Condens. Matter Phys.* **2021**, *12*, 155.
[12] S. Kaur, G. M. Weerasekare, R. J. Stewart, *ACS Appl. Mater. Interfaces.* **2011**, *3*, 941.
[13] E. Ban, A. Kim, *Int. J. Pharm.* **2022**, *624*, 122058.
[14] Y. J. Oh, I. H. Cho, H. Lee, K.-J. Park, H. Lee, S. Y. Park, *Chem. Commun.* **2012**, *48*, 11895.
[15] K. A. Black, D. Priftis, S. L. Perry, J. Yip, W. Y. Byun, M. Tirrell, *ACS Macro Lett.* **2014**, *3*, 1088.
[16] X. Mi, W. C. B. McTigue, P. U. Joshi, M. K. Bunker, C. L. Heldt, S. L. Perry, *Biomater. Sci.* **2020**, *8*, 7082.
[17] J. T. Overbeek, M. J. Voorn, *J. Cell. Physiol.* **1957**, *49*, 7.
[18] P. Zhang, K. Shen, N. M. Alsaifi, Z.-G. Wang, *Macromolecules* **2018**, *51*, 5586.
[19] Y. Liu, B. Momani, H. H. Winter, S. L. Perry, *Soft Matter* **2017**, *13*, 7332.
[20] M. Radhakrishna, K. Basu, Y. Liu, R. Shamsi, S. L. Perry, C. E. Sing, *Macromolecules* **2017**, *50*, 3030.
[21] L. Li, S. Srivastava, M. Andreev, A. B. Marciel, J. J. de Pablo, M. V. Tirrell, *Macromolecules* **2018**, *51*, 2988.
[22] E. Spruijt, A. H. Westphal, J. W. Borst, M. A. Cohen Stuart, J. van der Gucht, *Macromolecules* **2010**, *43*, 6476.
[23] J. Lou, S. Friedowitz, J. Qin, Y. Xia, *ACS Cent. Sci.* **2019**, *5*, 549.
[24] A. E. Neitzel, Y. N. Fang, B. Yu, A. M. Rumyantsev, J. J. De Pablo, M. V. Tirrell, *Macromolecules* **2021**, *54*, 6878.
[25] Q. Wang, J. B. Schlenoff, *Macromolecules* **2014**, *47*, 3108.
[26] J. Wang, M. Abbas, Y. Huang, J. Wang, Y. Li, *Commun. Chem.* **2023**, *6*, 243.
[27] J. Fu, H. M. Fares, J. B. Schlenoff, *Macromolecules* **2017**, *50*, 1066.
[28] R. A. Ghostine, R. F. Shamoun, J. B. Schlenoff, *Macromolecules* **2013**, *46*, 4089.
[29] M. Yang, Z. A. Digby, J. B. J. M. Schlenoff, *Macromolecules* **2020**, *53*, 5465.
[30] Y. Luo, M. Gu, C. E. Edwards, M. T. Valentine, M. E. Helgeson, *Soft Matter* **2022**, *18*, 3063.
[31] S. Alberti, A. Gladfelter, T. Mittag, *Cell* **2019**, *176*, 419.
[32] K. Murakami, S. Kajimoto, D. Shibata, K. Kuroi, F. Fujii, T. Nakabayashi, *J. Chem. Sci.* **2021**, *12*, 7411.
[33] H. M. Fares, A. E. Marras, J. M. Ting, M. V. Tirrell, C. D. Keating, *Nat. Commun.* **2020**, *11*, 5423.
[34] Y. Maeda, H. Yamamoto, I. Ikeda, *Macromolecules* **2003**, *36*, 5055.
[35] S. Choi, S. Y. Chun, K. Kwak, M. J. P. Cho, *Phys. Chem. Chem. Phys.* **2023**, *25*, 9051.
[36] I. Chourpa, V. Ducel, J. Richard, P. Dubois, F. Boury, *Biomacromolecules* **2006**, *7*, 2616.
[37] N. Arfin, V. Aswal, H. Bohidar, *RSC Adv.* **2014**, *4*, 11705.
[38] M. Matsumoto, T.-A. Asoh, T. Shoji, Y. Tsuboi, *Langmuir* **2021**, *37*, 2874.
[39] X. Gao, X. Li, W. Min, *J. Phys. Chem. Lett.* **2023**, *14*, 5701.
[40] M. P. Corujo, P. Michal, R. Wesson, D. P. Amarasinghe, A. Rodger, N. P. Chmel, *J. Spectrosc.* **2022**, *2022*, 1928091.
[41] M. D. Duncan, J. Reintjes, T. Manuccia, *Opt. Lett.* **1982**, *7*, 350.
[42] A. Zumbusch, G. R. Holtom, X. S. Xie, *PRL* **1999**, *82*, 4142.
[43] C.H. Camp Jr, M. T. Cicerone, *Nat. Photon.* **2015**, *9*, 295.
[44] E. Ploetz, S. Laimgruber, S. Berner, W. Zinth, P. Gilch, *Appl. Phys. B* **2007**, *87*, 389.
[45] C. W. Freudiger, W. Min, B. G. Saar, S. Lu, G. R. Holtom, C. He, J. C. Tsai, J. X. Kang, X. S. Xie, *Science* **2008**, *322*, 1857.
[46] D. W. McCamant, P. Kukura, R. A. Mathies, *Appl. Spectrosc.* **2003**, *57*, 1317.
[47] L. Czerwinski, J. Nixdorf, G. Di Florio, P. Gilch, *Opt. Lett.* **2016**, *41*, 3021.
[48] F. J. Morin, M. L. Puppo, J. E. Laaser, *Soft Matter* **2021**, *17*, 1223.
[49] J. Durig, C. Pate, *Spectrochim. Acta. A. Mol. Biomol. Spectrosc.* **1972**, *28*, 1031.
[50] D. M. Carey, G. M. Korenowski, *J. Chem. Phys.* **1998**, *108*, 2669.
[51] H.-C. Chen, H.-C. Lin, H.-H. Chen, F.-D. Mai, Y.-C. Liu, C.-M. Lin, C.-C. Chang, H.-Y. Tsai, C.-P. Yang, *Sci. Rep.* **2014**, *4*, 4425.
[52] H. Edwards, D. Brown, J. Dale, S. Plant, *Vib. Spectrosc.* **2000**, *24*, 213.
[53] L. van Westerveld, J. E. Sayed, M. de Graaf, A. H. Hofman, M. Kamperman, D. Parisi, *Soft Matter* **2023**, *19*, 8832.
[54] I. A. Oxton, O. Knop, M. Falk, *Can. J. Chem.* **1975**, *53*, 2675.
[55] G. Zundel, *Angew. Chem. Int. Ed.* **1969**, *8*, 499.
[56] U. M. Bhalerao, J. Acharya, A. K. Halve, M. P. Kaushik, *RSC Adv.* **2014**, *4*, 4970.
[57] D. Traficante, *Concepts Magn. Reson.* **1991**, *3*, 83.
[58] W. B. Schwartz, A. S. Relman, *NEJM* **1963**, *268*, 1382.
[59] H. Maeda, T. Michiue, T. Ishikawa, *Encyclopedia Of Forensic And Legal Medicine*, Second Edition, London, Elsevier **2016**, pp. 32–42.
[60] P. W. Atkins, J. De Paula, J. Keeler, *Atkins' Physical Chemistry*. Oxford, Oxford university press **2023**.
[61] E. Spruijt, J. Sprakel, M. A. C. Stuart, J. van der Gucht, *Soft Matter* **2010**, *6*, 172.
[62] L. Fisher, E. Mitchell, N. Parker, *J. Food Sci.* **1985**, *50*, 1201.
[63] V. A. Pigareva, I. N. Senchikhin, A. V. Bolshakova, A. V. Sybachin, *Polymers* **2022**, *14*, 1247.
[64] B. Marx, L. Czerwinski, R. Light, M. Somekh, P. Gilch, *J. Raman Spectrosc.* **2014**, *45*, 521.
[65] M. Lipkin, J. Nixdorf, P. Gilch, *Opt. Lett.* **2020**, *45*, 4204.
[66] P. Kukura, D. W. McCamant, R. Mathies, *Annu. Rev. Phys. Chem.* **2007**, *58*, 461.
[67] A. A. Green, M. Berman, P. Switzer, M. D. Craig, *IEEE Trans. Geosci. Remote Sens.* **1988**, *26*, 65.
[68] P. Hansen, B. Jaumard, *Math. Program.* **1997**, *79*, 191.
[69] T. Bocklitz, T. Meyer, M. Schmitt, I. Rimke, F. Hoffmann, F. von Eggeling, G. Ernst, O. Guntinas-Lichius, J. Popp, *APL Photonics* **2018**, *3*, 092404.

Manuscript received: March 24, 2025
Version of record online: April 30, 2025